The International Journal of Advanced Manufacturing Technology (2018) 96:2671–2685
https://doi.org/10.1007/s00170-018-1797-0

ORIGINAL ARTICLE

# Analytical cutting model for a single fiber to investigate the occurrences of the surface damages in milling of CFRP

Fei Su [1,2] · Juntang Yuan [3] · Fujian Sun [1,2] · Zhenhua Wang [3] · Zhaohui Deng [1,2]

Received: 28 November 2017 / Accepted: 12 February 2018 / Published online: 24 February 2018


**Abstract**

The edge milling process of carbon fiber-reinforced plastics (CFRPs) is often accompanied by delamination and burrs on slot edges of the top layer. These damages impact on processing quality, processing efficiency, strength, and fatigue life of the materials, etc. To investigate the occurrence of these damages, the analytical cutting model for a single fiber of the top layer is established based on the Winkler elastic foundation beam theory. The critical fiber cutting angles and the corresponding engagement angles with different initial fiber orientations are predicted. Then, the milling experiments with the initial fiber orientations $\theta_0 = 90°$ are carried out. The results show that the occurrences of the burrs and delamination can be correctly predicted. The suitable initial fiber orientations are chosen in the range from 30 to 60° for the smoother slot edges. There are two burr occurrence zones (BOZs) when $\theta_0 = 90°$. The delamination-inhibited zone (DIZ) is usually in the burr occurrence zone (BOZ).

**Keywords** Carbon fiber-reinforced plastic (CFRP) · Burrs · Delamination · Elastic foundation beam · Fiber orientation

## 1 Introduction

Carbon fiber-reinforced plastic (CFRP) is utilized more and more widely in aviation, aerospace, automotive, and defense industries due to its high specific strength, high specific stiffness, and good corrosion resistance [1–5]. In order to reach the required geometry tolerances and edge quality of the near net shape parts produced with CFRP composites, all the parts have to undergo various classical production processes, such as milling and drilling. Generally, the edge milling process is considered as one of the most common finishing operations in the industrial applications [6–8].

This is an original paper which has neither previously, nor simultaneously, in whole or in part been submitted anywhere else.

✉ Fei Su
sfeihe@163.com

1 Hunan Provincial Key Laboratory of High Efficiency and Precision Machining of Difficult-to-Cut Material, Hunan University of Science and Technology, Xiangtan 411201, China

2 Intelligent Manufacturing Institute of HNUST, Hunan University of Science and Technology, Xiangtan 411201, China

3 School of Mechanical Engineering, Nanjing University of Science and Technology, Nanjing 210094, China

However, CFRP composites are difficult-to-cut materials due to their inherent inhomogeneous and anisotropic mechanical properties [9, 10]. As such, a variety of damages occur on the top layer of the machined specimens during the edge milling of CFRP, such as burrs, fiber pull-out, delamination, and other invisible damages, as well as the tool will be severely worn [11–15]. These problems will have a direct impact on the processing quality, the manufacturing efficiency, the strength fatigue life of materials, etc. The delamination is regarded as the most critical one, because it can considerably reduce the stiffness and the load-carrying capacity of the mechanical parts [7, 16]. Furthermore, the burrs are the most frequent surface damage during edge milling of CFRP laminates [6–8], and their appearance may cause several problems. For example, the cost and the time of production will be increased due to additional machining (e.g., the removal of burrs, deburring), and the safety of the CFRP composite parts will be degraded [6–8]. Therefore, the expensive CFRP composite parts may be rejected at the last stage of their production cycle [6–8].

Until now, lots of researches have been done to investigate the factors influencing the burrs or the delamination to search for clarity about how to reduce burr and delamination sizes [7]. The formations of the burrs and the delamination can be directly influenced by the damages of the fiber and the matrix (e.g., fiber bucking and rupture, matrix crushing, and cracking) during the cutting of CFRP. Nevertheless, the fiber orientation is the critical factor affecting these damages [17]. Thus, many researchers have found that the fiber orientation has a significant effect on the milled damages of the milling surface (e.g., burrs and delamination). Colligan et al. [18, 19] found that the laminate top layer delamination appeared in three fundamental types depending on the fiber orientation. For example, the type I was that the surface fibers were broken and removed for some distance from the trimmed edge, and this type was most common in the 45 and 90° fiber orientations. The type II delamination was accompanied by some uncut fibers that protruded from the trimmed edge, and this type mostly appeared in the 135°. Ghafarizadeh et al. [9] proved that the extension of machining damage (e.g., cracking damage and burrs) significantly depended on the fiber orientation during the flat end milling of unidirectional CFRP. According to Hintze et al. [6], there were two kinds of delamination effects, i.e. generation and propagation. They found that the delamination and the fiber overhangs (or burrs) occurred where the fibers were initially cut in a critical cutting angle range, and any fiber protrusion was associated with delamination [6, 8, 16]. Additionally, they proposed an analytical model for the development of fiber protrusions [16]. Zhou et al. [20] confirmed that the fiber tended to be bent instead of being fractured when the actual bending radius was larger than the minimum bending radius, then the burrs occurred in the fiber cutting angle of the range from 90 to 180°. Voss et al. [8] presented the distributions of the critical cutting zone for different fiber orientations by conducting a number of milling experiments. Islam et al. [21] presented a simple and efficient framework (e.g., up-milled and down-milled) for understanding and predicting the occurrence of the damages in different fiber orientations during milling of CFRP.

Similarly, it was well-known that the processing parameters and the tool edge sharpness or cutting edge radius had a significant effect on the milled damage. Davim and Reis [22] established a multiple regression model to investigate the influences of the processing parameters (i.e., cutting velocity and feed rate) on the surface delamination in milling CFRP laminate plates, and they found that the feed rate presented the highest statistical and physical influence on delamination (larger than 80%). Sheikh-Ahmad et al. [19] found that both of the process parameters (e.g., spindle speed, feed rate) and the fiber orientation had a significant influence on the occurrence of delamination. Chibane et al. [23] and Ömer et al. [24] found that the damages on the machined surfaces increased with increasing cutting speed and feed rate. Wang et al. [7] expounded the effect of the cutting edge radius on the burr formation. It was illustrated that the burrs were prone to form in the fiber cutting angle range from 0 to 90° when a cutter with a large cutting edge radius was used. Ghidossi et al. [25] found that an important reason for the occurrence of the burrs in edge milling was the increase of the cutting edge radius.

All these existing literatures attempt to explore the key factors influencing on the damages or to reveal the mechanism of formation of these damages in order to obtain good surface quality with small damages. However, there are few references on the mechanical model employed to analyze the mechanism of milling damage formation. In this study, in order to better understand the mechanism of milling damage formation, an analytical cutting model for a single fiber of the top layer is established based on the Winkler elastic foundation beam theory. Combining the predictions and the experimental results, the occurrence of the burrs and delamination are studied. The conclusions obtained in this study are useful for understanding the effects of the major factors on the damage (i.e., burrs and delamination) formation during milling CFRP, as well as predicting the occurrence of these damages.

## 2 Modeling of the cutting-induced surface damage

### 2.1 Formation of the cutting-induced surface damage

Owing to a lack of constraint effects on the surface fibers, the fibers on the top layer are bent both in the laminate plane and perpendicular to the laminate plane because of the pushing effect of the cutters during the milling of CFRP. The fibers can evade the cutting edge because of this bending. As a result, some defects, such as burrs and delamination, appear at the trimmed edges.

In general, the fiber-cutting angle changes continuously as the tool rotates during the milling. Then, the removal mechanism of the fiber is different in different rotation angles of the cutter; as a result, the occurrences of the burrs and the delamination show regular changes with the rotation angle of the cutter. In order to analyze the cutting process of surface fibers, the cutting model of a single fiber is analyzed. Numerous experimental studies have shown that the fibers are squeezed by the cutting force $P_n$ in the cutting direction, as well as supported by the uncut layers of the laminate plane in front of the cutters. Simultaneously, the cutting force $P_t$ perpendicular to the laminate plane leads to the vertical buckling distortions of the fibers. The cutting process is illustrated in Fig. 1.

In order to deeply investigate this cutting model, the cutting processes of a single fiber in different rotation angles of the cutter are analyzed as a tooth of the cutter rotates a single revolution. The fibers' brittle fracture usually occurs in the tool–fiber contact area during the rapid contact between the fiber and the tool [26]. However, the top layer fibers often are only bent and not easily fractured in the tool–fiber contact area because of the phenomenon that the fibers avoid the tool. Thus, it is assumed that the fiber breaking points is not in the tool–fiber contact area. For the selected fiber, they are cut little by little in milling process, and each cut can be treated

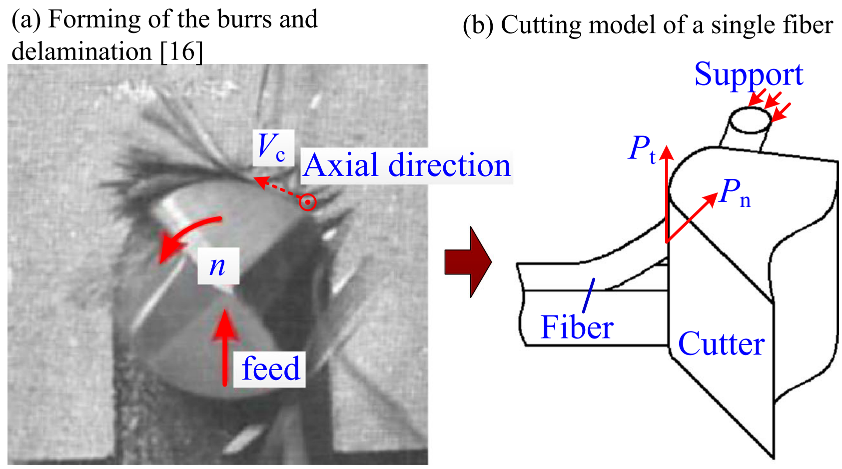


**Fig. 1** Cutting process and the cutting forces

as an independent orthogonal cutting process [26–29]. The cutting process usually is highly dependent on the fiber-cutting angle $\varphi$ and the tool-rake angle $\gamma_0$. The fiber-cutting angle $\varphi$ is measured anticlockwise from the fiber to the cutting-speed direction. Here, two possible scenarios are considered as follows.

(1) When $0 < \varphi \leq \gamma_0 + \pi/2$

It is assumed that the tool–fiber contact point is the contact point between the fiber end and the tool nose. Also, the tool–fiber contact point is in the rake face or at the arc edge of the blunt round near the rake face. The distance from the contact point to the fiber root will be defined as $\Delta\delta$. The fibers on the top layer are bent both in and perpendicular to the laminate plane as the cutter moves forward. As a result, the contact point is gradually moving toward the flank face and upward along the fiber simultaneously. When the fiber is tangent to the flank face by bending, the tool moves gradually away from this selected fiber and loses the cutting effect. Then, the fiber will not be cut off if the fiber bending failure has not yet occurred before this, which can result in the formation of burrs. The bending angle will reach its maximum value when the fiber was tangent to the flank face. It can be found that this maximum bending angle is equal to the fiber-cutting angle. The slip displacement of the contact point is $\Delta w$, and the bending length of the fiber in the laminate plane is $L_m$. All these parameters are shown in Fig. 2. The maximum bending angles with different fiber-cutting angles are shown in Fig. 3. With increasing fiber-cutting angle, both the slip displacement $\Delta w$ and the maximum bending angle increase, resulting in an increase in possibility of the fiber fracture. It is assumed that the contact point is right at the point of tangency of the rake face and the blunt round when $\varphi = \gamma_0 + \pi/2$, and the height of this contact point reaches the maximum value ($r_e(1 + \sin\gamma_0)$).

In fact, the tool–fiber contact point may be in the middle part of the selected fiber in actual processing. It is also assumed that the fiber is not broken at the contact point. Then, the contact point is also gradually moving upward along the fiber and away from the fiber root simultaneously. The bending part of the fiber will lose the supporting effect of the uncut layers due to this upward bending. Therefore, this situation still can be argued that the contact point is at the fiber end.

(2) When $\gamma_0 + \pi/2 < \varphi$

Similarly, it is assumed that the tool–fiber contact point is at the fiber end. The contact point is gradually moving toward the flank face and approaching the fiber root simultaneously (as shown in Fig. 2). When the fiber was tangent to the flank face, the fiber is bent to its limit position. After this, the cutter loses the cutting effect for the selected fiber. To simplify the complex cutting process, the extreme position will only be analyzed as following. During the movement of the contact point, the total displacement of the contact point is the vector sum of the slip displacement in and perpendicular to the laminate plane (as illustrated in Fig. 2). Within the laminate plane, the fiber is bent and supported by the uncut layers during the cutting. Thus, the in-plane bending of the fiber will be considered as the bending of a semi-infinite elastic foundation beam, whose distance of the stress point deviating from the beam end is $c$. When the fiber is bent to its limit position, the fiber–tool contact point is at the fiber root, namely, $c = \Delta\delta$, as seen in Figs. 2 and 3. Likewise, with the fiber-cutting angle increasing, the possibility of the fiber fracture increases. Additionally, it is found that there are two cases when $\gamma_0 + \pi/2 < \varphi$, i.e. the cutting thickness $h$ is greater or lesser than $r_e(1 + \sin\gamma_0)$.

According to the above analysis of the cutting process with different fiber-cutting angles, the distance from the contact point to the fiber root $\Delta\delta$ can be determined by the fiber-cutting angle $\varphi$ (as shown in Eq. (1)). Also, the fiber

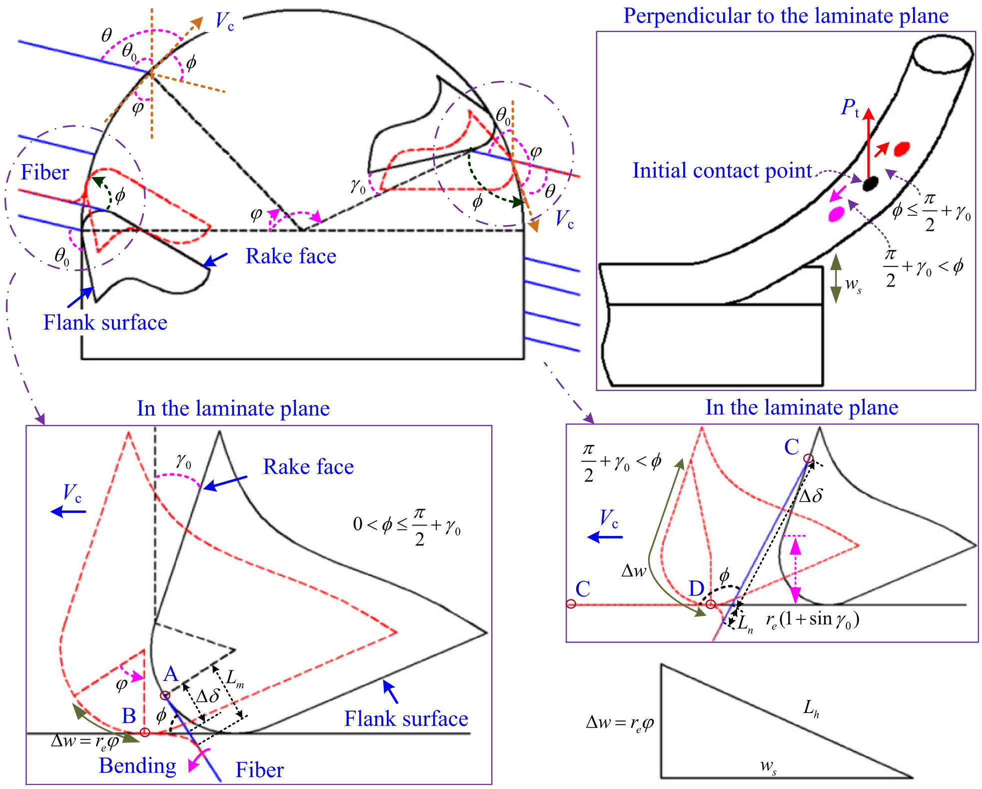


**Fig. 2** Analysis of the cutting process with different fiber-cutting angles

orientation angle $\theta$ can be clearly determined by the initial fiber orientation angle $\theta_0$ and the engagement angle $\varphi$ (as shown in Eq. (2)).

$$\Delta\delta = \begin{cases} \dfrac{r_e(1-\cos\phi)}{\sin\phi} & \left(0 < \phi \le \dfrac{\pi}{2} + \gamma_0\right) \\ \dfrac{h}{\sin\phi} = \dfrac{f_z \sin\varphi}{\sin\phi} & \left(\dfrac{\pi}{2} + \gamma_0 < \phi\right) \end{cases} \tag{1}$$

$$\theta = \begin{cases} \theta_0 + \varphi & (0 \le \theta_0 + \varphi < \pi) \\ \theta_0 + \varphi - \pi & (\pi \le \theta_0 + \varphi) \end{cases} \tag{2}$$

The fiber orientation angle $\theta$ is complementary with the fiber-cutting angle $\varphi$, namely $\theta + \varphi = \pi$. The relationship among $\varphi$, $\theta_0$, and $\varphi$ can be written as follows

$$\phi = \begin{cases} \pi\text{-}(\theta_0 + \varphi) & (0 \le \theta_0 + \varphi < \pi) \\ 2\pi - (\theta_0 + \varphi) & (\pi \le \theta_0 + \varphi) \end{cases} \tag{3}$$

where $\gamma_0$, $\theta_0$, $\theta$, and $\varphi$ are the tool rake angle, the initial fiber orientation angle, the fiber orientation angle, and the engagement angle, respectively. The symbol $\varphi$ is the fiber-cutting angle which is equal to the maximum bending angle.

## 2.2 Cutting model of the single fiber on the surface

The elastic foundation beam theory has already been used in modeling to research the chip formation mechanism [5]. The selected fiber is wrapped and supported by the surrounding uncut materials, and the length of the selected fiber stressed area is very short. Then, the support force of the uncut materials is uniformly distributed on the selected fiber. Therefore, the fiber is regarded as a beam structure, and the part of the composite that supports the fiber can be regarded as an elastic foundation. The fiber deformation is considered as one bending problem of the beam on elastic foundation. Thereby, within the laminate plane, the fiber is supported by the surrounding materials, so the fiber bending is regarded as the bending of a semi-infinite elastic ground beam. The fiber bending perpendicular to the laminate plane is also simplified as the bending of a beam which is under a tensile load.

In order to establish the rational mechanical model, the following assumptions need to be made because of the complicated and changeable tool geometry and cutting conditions.

1. Plastic deformation of the material is negligible, and no matrix extension or compression occurs.
2. Transverse shear effect of the resin matrix is negligible.
3. Shear stress in fiber is negligible, and the bending fracture of the fiber is only considered.
4. The width of the workpiece is equal to the diameter of the fiber.
5. The surrounding materials are assumed as the homogeneous and isotropic elastic materials.

Based mainly on mechanics theory of bending distortion, the forming mechanism of the burrs and the delamination will

**Fig. 3** Maximum bending angle with different fiber-cutting angles

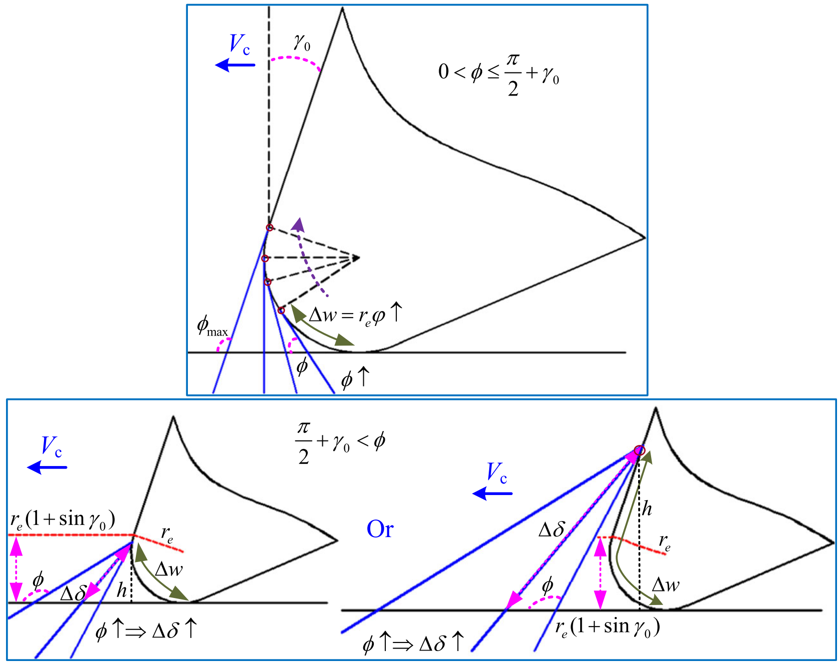


be studied in this paper. Moreover, theoretically, a high bending moment occurs at the locations of the small fiber bending radius, especially when the fiber orientation angle $\theta > 90°$. The minimal fiber bending radius can be determined by Eq. (4) [16]. However, the size of the burrs during the milling has a certain randomness; as a result, the fiber diameter or the bundle thickness $d_{\text{fiber}}$ is not easy to be determined. To simplify the modeling process, the effects of the helix angle, the cutting vibration, the cutting speed, and the bending radius are negligible in this study. All these effects will be discussed in detail in the further studies.

$$r_{\min} = \frac{1}{2}\left(\frac{1}{\xi_b}-1\right)d_{fiber} \tag{4}$$

$r_{\min}$, $\xi_b$, and $d_{\text{fiber}}$ are the minimal fiber bending radius, the strain rate, and the fiber diameter or the bundle thickness, respectively.

To further reveal the formation mechanism of the burrs and delamination during milling, the cutting model of a single fiber is established at different fiber-cutting angles (i.e., $0 < \varphi \leq \gamma_0 + \pi/2$ and $\gamma_0 + \pi/2 < \varphi$), with Winkler's foundation model.

① Elastic foundation modeling of cutting a single fiber when $0 < \varphi \leq \gamma_0 + \pi/2$

(a) Fiber bending model in the laminate plane when $0 < \varphi \leq \gamma_0 + \pi/2$

The tool–fiber contact point is at the fiber end, and the fiber-bending model is illustrated in Fig. 4. The selected fiber is divided into two segments due to the varying supporting conditions along the fiber axis. The 1st segment OA is only supported by the uncut layers behind this fiber, because the point A is the onset point of the debonding. The 2nd segment AB is supported by the rest of the composite and is bonded by the resin matrix simultaneously. In order to simplify the modeling process, the Winkler's foundation model will be used to solve the bending of the beam on elastic foundation. According to the Winkler's foundation model, the reaction force $P_{\text{m}}$ from the supporting materials per unit length and the bonding force $q_{\text{b}}$ are expressed as $P_m = k_m w(x)$ and $q_b = k_b w(x)$, respectively. The governing differential equation for the second segment AB [12, 13, 26] can be obtained as follows:

$$E_f I_f \frac{d^4 w(x)}{dx^4} + (k_m + k_b)w(x) = 0 \tag{5}$$

where $k_{\text{m}}$, $k_{\text{b}}$, $E_f$, and $I_f$ are the modulus of the supporting composite which can be treated as an equivalent homogeneous material (EHM), the equivalent modulus of the fiber-matrix bonding, Young's modulus, and the moment of inertia of the fiber, respectively.

The bending of the 1st segment OA will be considered and its governing differential equation is the same as in Eq. (5), but $k_{\text{b}} = 0$. Its general deformation can be described as follows [26]:

$$w(x) = e^{\lambda x}(c_1\cos\lambda x + c_2\sin\lambda x) + e^{-\lambda x}(c_3\cos\lambda x + c_4\sin\lambda x) \tag{6}$$

where $\lambda = \sqrt[4]{\frac{k_m b}{4E_f I_f}}$, $I_f = \frac{\pi D^4}{64}$, and $c_1$–$c_4$ are constants of integration.

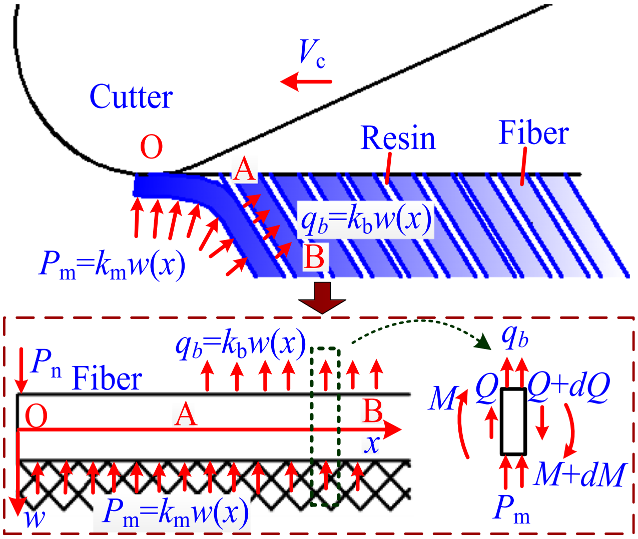


**Fig. 4** Fiber-bending model in the laminate plane ($0<\varphi\le\gamma_0+\pi/2$)

It can be obtained $c_1=c_2=0$ in Eq. (6), owing to the boundary condition at the fiber bottom ($x\to\infty$, $w\to 0$). According to the boundary condition at the fiber top ($x=0$), the other two constants $c_3$ and $c_4$ can be resolved as $c_4=0$ and $c_3=\frac{P}{2\lambda^3 E_f I_f}$. Then, the deflection of the fiber can be written as [26]:

$$w(x)=\frac{2P\lambda e^{-\lambda x}}{kb}\cos(\lambda x). \tag{7}$$

Thereby, the slope of deflection can be derived straightforwardly, as shown in Eq. (8).

$$\vartheta(x)=w^{'}(x)=\frac{2P\lambda^2 e^{-\lambda x}}{kb}(\cos(\lambda x)+\sin(\lambda x)) \tag{8}$$

According to the analyses of the cutting process, it can be known $x=\Delta\delta$ and $\vartheta(\Delta\delta)=\phi$ when the fiber is tangent to the flank face. Therefore, the load $P_n$ and the bending moment $M$ when $0<\varphi\le\gamma_0+\pi/2$ can be resolved as:

$$\begin{cases} P_n=\dfrac{k_m b\phi e^{\lambda\Delta\delta}}{2\lambda^2[\cos(\lambda\Delta\delta)+\sin(\lambda\Delta\delta)]} \\ M=\dfrac{4E_f I_f P\lambda^3 e^{-\lambda x}\sin(\lambda x)}{k_m b} \end{cases}. \tag{9}$$

Based on the knowledge of material mechanics [30], the bending moment of the cross-section reaches the maximum value when the shear force $Q(x)=0$, namely $\frac{dM}{dx}=0$. The maximum deflection of the fiber can be derived as $L_1=\pi/4\lambda$ because $Q=\frac{dM}{dx}=-EIw^{'''}(x)$ and $w^{'''}(x)=0$. Therefore, the maximum bending moment of the cross-section can be described as:

$$\begin{aligned} M_{N\max}=M(L_1)&=\frac{4E_f I_f P\lambda^3 e^{-\lambda L_1}\sin(\lambda L_1)}{kb} \\ &=\frac{2\lambda E_f I_f\phi e^{\lambda(\Delta\delta-L_1)}\sin(\lambda L_1)}{\cos(\lambda\Delta\delta)+\sin(\lambda\Delta\delta)} \end{aligned} \tag{10}$$

(b) Fiber bending model in the vertical plane when $0<\varphi\le\gamma_0+\pi/2$

The tool–fiber contact point is at the fiber end, and the fiber-bending model in the plane which is perpendicular to the laminate plane is illustrated in Fig. 5. The force $P_t$ is loaded at point A. The selected fiber is also divided into two segments due to the varying supporting conditions along the fiber axis. The 1st segment AO is pulled by the vertical upward force and has no adhesion force, because the point O is the onset point of the debonding. However, the 2nd segment OB is bonded by the resin matrix. According to the Winkler's foundation model, the reaction force $P_m$ from the matrix per unit length is expressed as $P_m=k_m w(x)$. Similarly, the governing differential equation for the 1st segment AO is the same as in Eq. (5), but $k_b=k_m=0$. Its general deformation can be described as [31]:

$$w(x)=b_1x^3+b_2x^2+b_3x+b_4 \tag{11}$$

where $b_1$–$b_4$ are constants of integration.

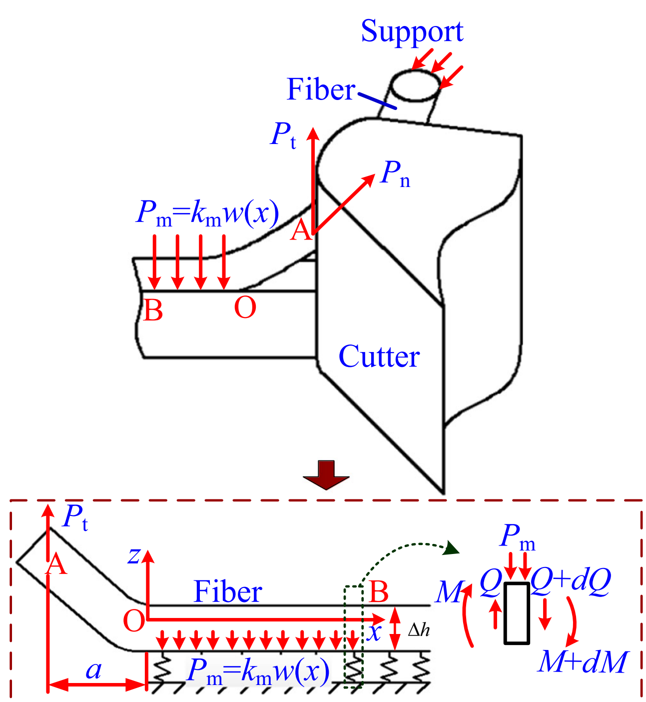


**Fig. 5** Bending model in the vertical plane ($0<\varphi\le\gamma_0+\pi/2$)

Likewise, the governing differential equation for the 2nd segment OB is the same as in Eq. (5), but $k_b = 0$. Its general solution is the same as in Eq. (6). According to the boundary conditions and the continuity of the fiber deflection, the fiber deflection of the 2nd segment OB can be obtained as [31]:

$$w(x) = \frac{P_\Delta a e^{-\lambda x}}{2E_f I_f \lambda^2}(\cos(\lambda x)\text{-}\sin(\lambda x)) \tag{12}$$

where $P_\Delta = \mu P = \frac{\mu k b \phi e^{\lambda\Delta\delta}}{2\lambda^2[\cos(\lambda\Delta\delta)+\sin(\lambda\Delta\delta)]}$ and $a = \Delta\delta$.

Similarly, the bending moment of the cross-section reaches the maximum value when the shear force $Q(x) = 0$. Then, the maximum deflection of the fiber can be derived as $\Delta L = \pi/2\lambda$ because $Q = \frac{dM}{dx} = \text{-}EIw'''(x)$ and $w'''(x) = 0$. Therefore, the maximum bending moment of the cross-section can be described as:

$$\begin{aligned} M_{z\max} &= P_\Delta(\Delta\delta + \Delta L) \\ &= \frac{\mu k b \phi e^{\lambda\Delta\delta}}{2\lambda^2[\cos(\lambda\Delta\delta)+\sin(\lambda\Delta\delta)]}(\Delta\delta + \Delta L) \end{aligned} \tag{13}$$

Based on the above theory model, the total bending moment is the vector sum of that in the laminate plane and that in vertical plane, as described in Eq. (14).

$$\begin{aligned} M_{\max} &= \sqrt{M_{z\max}^2 + M_{N\max}^2} \\ &= \sqrt{\left[\frac{\mu k b \phi e^{\lambda\Delta\delta}}{2\lambda^2[\cos(\lambda\Delta\delta)+\sin(\lambda\Delta\delta)]}(\Delta\delta+\Delta L)\right]^2 + \left[\frac{2\lambda E_f I_f \phi e^{\lambda(\Delta\delta - L)}\sin(\lambda L_1)}{\cos(\lambda\Delta\delta)+\sin(\lambda\Delta\delta)}\right]^2} \\ &= \frac{\phi e^{\lambda\Delta\delta}}{2\lambda^2[\cos(\lambda\Delta\delta)+\sin(\lambda\Delta\delta)]}\sqrt{[\mu k b(\Delta\delta+\Delta L)]^2 + \left[4\lambda^3 E_f I_f e^{-\lambda L}\sin(\lambda L_1)\right]^2} \end{aligned} \tag{14}$$

The neutral layer is through the fiber axis because the fiber shape is cylindrical. The neutral layer is regarded as the interface. Thus, the protrudent side is in tension, and the indentation side is in compression. According to the knowledge of material mechanics, the maximum tensile stress $\sigma$ occurs in the cross-section in which the bending moment reaches the maximum value, as well as at the point which is farthest away from the neutral layer. Then, the maximum tensile stress can be written as

$$\sigma = \frac{M_{\max} r_f}{I_f} = \frac{r_f \phi e^{\lambda\Delta\delta}}{2\lambda^2 I_f[\cos(\lambda\Delta\delta)+\sin(\lambda\Delta\delta)]} \sqrt{[\mu k b(\Delta\delta+\Delta L)]^2 + \left[4\lambda^3 E_f I_f e^{-\lambda L}\sin(\lambda L_1)\right]^2} \tag{15}$$

According to the maximum strength theory, when the maximum tensile stress exceeds its tensile strength (as shown in Eq. (16)), the fiber fractures and the fiber can be removed.

$$\sigma = \frac{r_f \phi e^{\lambda\Delta\delta}}{2\lambda^2 I_f[\cos(\lambda\Delta\delta)+\sin(\lambda\Delta\delta)]} \sqrt{[\mu k b(\Delta\delta+\Delta L)]^2 + \left[4\lambda^3 E_f I_f e^{-\lambda L}\sin(\lambda L_1)\right]^2} \geq \sigma_b \tag{16}$$

Therefore, the critical fiber cutting angle $\varphi_{CT1}$ when $0 < \varphi \leq \gamma_0 + \pi/2$ can be obtained. The fiber can be effectively removed if the fiber cutting angle exceeds the critical one (as written in Eq. (17)), before the fiber is tangent to the flank face.

$$\phi \geq \phi_{CT1} = \frac{2\sigma_b \lambda^2 I_f[\cos(\lambda\Delta\delta)+\sin(\lambda\Delta\delta)]}{r_f e^{\lambda\Delta\delta}\sqrt{[\mu k b(\Delta\delta+\Delta L)]^2 + \left[4\lambda^3 E_f I_f e^{-\lambda L}\sin(\lambda L_1)\right]^2}} \tag{17}$$

Besides, the maximum fiber deflection of the segment AO (as shown in Fig. 5), which is the total deflection caused by $P_n$ and $P_t$, can be obtained as follows:

$$w_{AO\max} = \frac{P_z a^3}{3E_1 I_f} + \frac{P_z a^2}{\lambda E_1 I_f} + \frac{P_z a}{2\lambda^2 E_1 I_f} \tag{18}$$

where $P_z$ is the total effect force of $P_n$ and $P_t$, $P_z = \sqrt{1+\mu^2}P$.

Thus, the flexibility $C$ of AO can be expressed as [32]:

$$C = \frac{w_{AO\max}}{P_z} = \frac{a^3}{3E_1 I_f} + \frac{a^2}{\lambda E_1 I_f} + \frac{a}{2\lambda^2 E_1 I_f}. \tag{19}$$

Consequently, according to the linear elastic fracture mechanics (LEFM) theory, the strain energy release rate of Mode I fracture along the fiber–matrix interface ($G_{IC}$) can be estimated as [32]:

$$\begin{aligned} G_I &= \frac{P_z^2 dC}{2bda} \\ &= \frac{P_z^2 a^2}{2E_1 I_f b}\left[1 + \frac{\sqrt[4]{6}}{3}\sqrt[4]{\frac{E_1}{E_2}}\left(\frac{\Delta h}{a}\right) + \frac{\sqrt{6}}{12}\sqrt{\frac{E_1}{E_2}}\left(\frac{\Delta h}{a}\right)^2\right]. \end{aligned} \tag{20}$$

The delamination cracking between the fiber and the matrix will occur when the strain energy release rate of Mode I fracture ($G_{IC}$) exceeds the critical one. On the contrary, the delamination cracking will not occur, and the following equation can be obtained as:

$$G_I = \frac{\left(\frac{\sqrt{1+\mu^2}kab\phi e^{\lambda\Delta\delta}}{2\lambda^2[\cos(\lambda\Delta\delta)+\sin(\lambda\Delta\delta)]}\right)^2}{2E_1 I_f b}\left[1 + \frac{\sqrt[4]{6}}{3}\sqrt[4]{\frac{E_1}{E_2}}\left(\frac{\Delta h}{a}\right) + \frac{\sqrt{6}}{12}\sqrt{\frac{E_1}{E_2}}\left(\frac{\Delta h}{a}\right)^2\right] \leq G_{Ic}. \tag{21}$$

The other critical fiber cutting angle $\varphi_{C1}$ when $0<\varphi\le\gamma_0+\pi/2$ can be obtained. The delamination cracking which caused by $P_n$ and $P_t$ will not occur if the fiber cutting angle is less than the critical one. This critical fiber cutting angle $\varphi_{C1}$ can be described as

$$\phi_{C1}\le\sqrt{\frac{8E_1I_fG_{Ic}\left[\lambda^2[\cos(\lambda\Delta\delta)+\sin(\lambda\Delta\delta)]\right]^2}{(1+\mu^2)k^2a^2be^{2\lambda\Delta\delta}\left[1+\frac{\sqrt[4]{6}}{3}\sqrt[4]{\frac{E_1}{E_2}}\left(\frac{\Delta h}{a}\right)+\frac{\sqrt{6}}{12}\sqrt{\frac{E_1}{E_2}}\left(\frac{\Delta h}{a}\right)^2\right]^2}}. \tag{22}$$

② Elastic foundation modeling of cutting a single fiber when $\pi/2+\gamma_0<\varphi$

(c) Fiber bending model in the laminate plane when $\pi/2+\gamma_0<\varphi$

The contact point is gradually moving toward the flank face and approaching the fiber root simultaneously. The extreme position which the fiber is tangent to the flank face will be analyzed. The bending model is indicated in Fig. 6. The point O is the contact point. Owing to the varying supporting conditions along the fiber axis, the fiber is divided into three segments, AO, OB, and BC, as illustrated in Fig. 6. The supporting condition of the 1st segment AO is the same as that of the 2nd segment OB, because the point B is the onset point of the debonding. Thereby, these two segments are only supported by the uncut layers behind the fiber. Thus, the 3rd segment BC is supported by the rest of the composite and bonded by the resin matrix simultaneously. Similarly, the governing differential equation of the 3rd segment BC and its general deformation are the same as in Eq. (5) and Eq. (6), respectively. Substituting $k_b=0$ into Eq. (5), the governing differential equation of the segment AB can be obtained, as shown in Eq. (23). Here, the study subject puts emphases on the bending of the segment AB. The deflection of this segment fiber can be given by engaged its governing differential equation and boundary conditions.

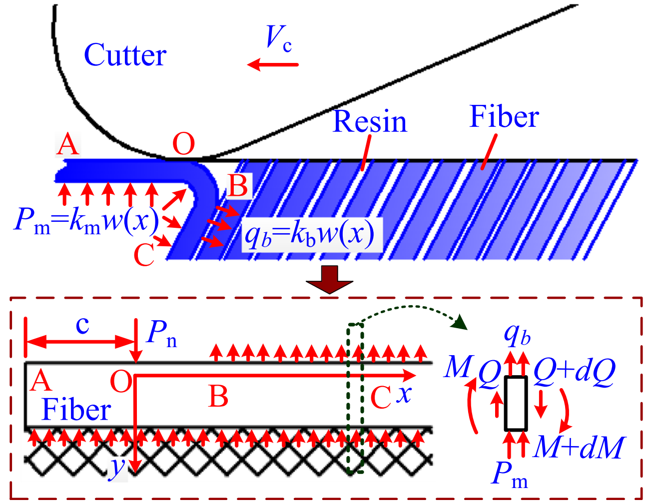


Fig. 6 Fiber-bending model in the laminate plane ($\pi/2+\gamma_0<\varphi$)

$$w(x)=\frac{2P\lambda e^{-\lambda x}}{kb}(\cos(\lambda|x|)+\sin(\lambda|x|))+\frac{P\lambda}{kb}\begin{pmatrix}e^{-\lambda c}\cos(\lambda c)e^{-\lambda(x+c)}\cos(\lambda(x+c))+\frac{1}{2}e^{-\lambda c}(\cos(\lambda c)-\sin(\lambda c))e^{-\lambda(x+c)}\cos(\lambda(x+c))\\-\frac{1}{2}e^{-\lambda c}(\cos(\lambda c)-\sin(\lambda c))e^{-\lambda(x+c)}\sin(\lambda(x+c))\end{pmatrix} \tag{23}$$

Next, the slope of deflection can be derived straightforwardly, as shown in Eq. (24).

$$w'(x)=-\frac{P\lambda^2}{kb}\left(2e^{-\lambda(2c+x)}\cos(\lambda c)\cos(\lambda(x+c))+e^{-\lambda(2c+x)}\cos(\lambda c)\sin(\lambda(x+c))-e^{-\lambda(2c+x)}\sin(\lambda c)\cos(\lambda(x+c))+4e^{-\lambda x}\sin(\lambda x)\right) \tag{24}$$

where $c=\Delta\delta$.

Attention will be focused on the fiber fracture below the cutter in the following sections, namely $x>0$; thereby, the bending moment can be expressed as

$$M=\frac{E_fI_fP\lambda^3}{kb}\begin{pmatrix}3e^{-\lambda(2c+x)}\cos(\lambda c)\sin(\lambda(x+c))+e^{-\lambda(2c+x)}\cos(\lambda c)\cos(\lambda(x+c))-e^{-\lambda(2c+x)}\sin(\lambda c)\sin(\lambda(x+c))\\-e^{-\lambda(2c+x)}\sin(\lambda c)\cos(\lambda(x+c))-4e^{-\lambda x}\cos(\lambda x)+4e^{-\lambda x}\sin(\lambda x)\end{pmatrix}. \tag{25}$$

In the same way, the bending moment $M$ reaches the maximum value when $\frac{dM}{dx}=0$, namely $w'''(x)=0$. The maximum deflection of the fiber can be derived as

$$L_2=\frac{1}{\lambda}\tan^{-1}\left(\frac{4+e^{-2\lambda c}-2e^{-2\lambda c}\cos(\lambda c)\sin(\lambda c)}{2e^{-2\lambda c}(\cos(\lambda c))^2}\right). \tag{26}$$

The contact point is at the fiber root when the fiber is tangent to the flank face, namely $x = 0$, and the slope of deflection is equal to $\varphi$.

$$w'(0) = \frac{P\lambda^2}{kb}\left(2e^{-2\lambda c}(\cos(\lambda c))^2\right) = \phi \tag{27}$$

Likewise, the load $P$ and the bending moment $M$ when $\gamma_0 + \pi/2 < \varphi$ can be resolved.

$$\begin{cases} P = \dfrac{\phi kb}{\lambda^2\left(2e^{-2\lambda c}(\cos(\lambda c))^2\right)} \\ M_{2\max} = \dfrac{E_f I_f \lambda\phi A_1}{\left(2e^{-2\lambda c}(\cos(\lambda c))^2\right)} \end{cases} \tag{28}$$

where $A_1 = 3e^{-\lambda(2c+L_2)}\cos(\lambda c)\sin(\lambda(L_2+c)) + e^{-\lambda(2c+L_2)}\cos(\lambda c)\cos(\lambda(L_2+c)) - e^{-\lambda(2c+L_2)}\sin(\lambda c)\sin(\lambda(L_2+c)) - e^{-\lambda(2c+L_2)}\sin(\lambda c)\cos(\lambda(L_2+c)) - 4e^{-\lambda L_2}\cos(\lambda L_2) + 4e^{-\lambda L_2}\sin(\lambda L_2)$ .

(d) Fiber bending model in the vertical plane ($\gamma_0 + \pi/2 < \varphi$)

The fiber bending model in the vertical plane when $\gamma_0 + \pi/2 < \varphi$ is the same as that one when $0 < \varphi \leq \gamma_0 + \pi/2$, while the force in the vertical plane alters. Here, the force can be expressed as:

$$P_{2\Delta} = \mu P = \frac{\mu\phi kb}{}\lambda^2\left(2e^{-2\lambda c}(\cos(\lambda c))^2\right) \tag{29}$$

So that, the maximum bending moment can be expressed by

$$\begin{aligned} M_{z\max} &= P_{2\Delta}(\Delta\delta + \Delta L) \\ &= \frac{\mu\phi kb}{}\lambda^2\left(2e^{-2\lambda c}(\cos(\lambda c))^2\right)(\Delta\delta + \Delta L) \end{aligned} \tag{30}$$

where $\Delta L = \frac{\pi}{2\lambda}$.

The total bending moment is described in Eq. (31).

$$\begin{aligned} M_{h\max} &= \sqrt{M_{z\max}^2 + M_{2\max}^2} \\ &= \sqrt{\left[\frac{\mu\phi kb}{}\lambda^2\left(2e^{-2\lambda c}(\cos(\lambda c))^2\right)(\Delta\delta + \Delta L)\right]^2 + \left[\frac{E_f I_f \lambda\phi A_1}{\left(2e^{-2\lambda c}(\cos(\lambda c))^2\right)}\right]^2} \\ &= \frac{\phi}{2\lambda^2 e^{-2\lambda c}(\cos(\lambda c))^2}\sqrt{[\mu kb(\Delta\delta + \Delta L)]^2 + \left(E_f I_f \lambda^3 A_1\right)^2} \end{aligned} \tag{31}$$

The maximum tensile stress is given by:

$$\sigma = \frac{M_{h\max} r_f}{I_f} = \frac{r_f\phi}{2\lambda^2 I_f e^{-2\lambda c}(\cos(\lambda c))^2}\sqrt{[\mu kb(\Delta\delta + \Delta L)]^2 + \left(E_f I_f \lambda^3 A_1\right)^2}. \tag{32}$$

With $\sigma = \frac{r_f\phi}{2\lambda^2 I_f e^{-2\lambda c}(\cos(\lambda c))^2}\sqrt{[\mu kb(\Delta\delta + \Delta L)]^2 + \left(E_f I_f \lambda^3 A_1\right)^2} \geq \sigma_b$, the critical fiber-cutting angle $\varphi_{CT2}$ when $\gamma_0 + \pi/2 < \varphi$ can be obtained.

$$\phi_{CT2} \geq \frac{2\sigma_b\lambda^2 I_f e^{-2\lambda c}(\cos(\lambda c))^2}{r_f\sqrt{[\mu kb(\Delta\delta + \Delta L)]^2 + \left(E_f I_f \lambda^3 A_1\right)^2}} \tag{33}$$

By the same token, the strain energy release rate of Mode I fracture ($G_{IC}$) can also be estimated by

$$\begin{aligned} G_I &= \frac{P_{2z}^2 a^2}{2E_1 I_f b}\left[1 + \frac{\sqrt[4]{6}}{3}\sqrt[4]{\frac{E_1}{E_2}}\left(\frac{\Delta h}{a}\right) + \frac{\sqrt{6}}{12}\sqrt{\frac{E_1}{E_2}}\left(\frac{\Delta h}{a}\right)^2\right] \\ &= \frac{\left(\frac{\sqrt{1+\mu^2}\phi kab}{2\lambda^2 e^{-2\lambda c}(\cos(\lambda c))^2}\right)^2}{2E_1 I_f b}\left[1 + \frac{\sqrt[4]{6}}{3}\sqrt[4]{\frac{E_1}{E_2}}\left(\frac{\Delta h}{a}\right) + \frac{\sqrt{6}}{12}\sqrt{\frac{E_1}{E_2}}\left(\frac{\Delta h}{a}\right)^2\right] \leq G_{Ic}. \end{aligned} \tag{34}$$

Furthermore, the other critical fiber-cutting angle $\varphi_{C2}$ when $\gamma_0 + \pi/2 < \varphi$ can be obtained.

$$\phi_{C2} \leq \sqrt{\frac{8E_1 I_f G_{Ic}\left[\lambda^2 e^{-2\lambda c}(\cos(\lambda c))^2\right]^2}{(1+\mu^2)k^2a^2b\left[1 + \frac{\sqrt[4]{6}}{3}\sqrt[4]{\frac{E_1}{E_2}}\left(\frac{\Delta h}{a}\right) + \frac{\sqrt{6}}{12}\sqrt{\frac{E_1}{E_2}}\left(\frac{\Delta h}{a}\right)^2\right]}} \tag{35}$$

The critical fiber-cutting angles (i.e., $\varphi_{CT1}$ and $\varphi_{CT2}$) for the two cases (i.e., $0 < \varphi \leq \gamma_0 + \pi/2$ and $\gamma_0 + \pi/2 < \varphi$) can be represented by the same symbol, $\varphi_{CT}$. The selected fiber will fracture under pure bending if the fiber-cutting angle exceeds the critical one during the milling. On the contrary, the selected fiber cannot be removed and turn into a burr. As a result, there formed a great number of burrs which can be called as the burr occurrence zone (BOZ), overall the cutting area. Analogously, the other critical fiber-cutting angles (i.e., $\varphi_{C1}$ and $\varphi_{C2}$) for the two cases (i.e., $0 < \varphi \leq \gamma_0 + \pi/2$ and $\gamma_0 + \pi/2 < \varphi$) can be represented by the same symbol, $\varphi_C$. The delamination cracking occurs between the fiber and the composite, if the fiber cutting angle is larger than the critical one. Then, the formation of the delamination is a regional phenomenon in the whole cutting area. Conversely, the delamination cracking can be inhibited. The range in which the delamination cracking can be depressed can be regarded as delamination-inhibited zone (DIZ).

## 3 Experimental approach

As a view to validate the theoretical model established in the previous sections, all the critical fiber cutting angles for the two cases with different initial fiber orientation were predicted. The occurrence of the damages with the initial fiber orientation $\theta_0 = 90°$ would be investigated in some milling tests in detail. The YG6X carbide mill with two straight flutes, a helix angle $\beta_b = 0°$, a rake angle $\gamma_0 = 15°$, a clearance angle $\alpha_0 = 10°$, a rounded edge radius $r_e = 15$ μm, and a diameter 6 mm were applied for the milling tests. Here, the milling length of each test was about 15–20 mm, and the tool wear could be ignored. The other material properties and the feed per tooth used for model predictions are listed in Table 1.

Woven CFRP composites are increasingly applied in different industrial sectors due to their some advantages comparing with the unidirectional laminates [35]. Moreover, the anisotropic behavior of the damages during the woven CFRP cutting is similar to that during the unidirectional CFRP. Therefore, a unidirectional carbon plain weave fabric/epoxy resin (T300/Epoxy) composite plate was applied in the experiments. The average thickness per layer was 0.2 mm, the total thickness was 10 mm, the width of a bundle of fiber was 2.5 mm, the fiber volume content was 60 ± 5%, and the average diameter of carbon fibers was 7–8 μm. The laminate density was 1.35 g/cm$^3$. All the milling experiments were carried out on KVC1050M NC vertical machining center without a coolant. A cutting depth ($a_p$) of 3 mm was adopted. The cutting speed ($V_c$) and the feed speed ($V_f$) were chosen in the range of 64–109 m/min (the selected interval was 15 m/min) and 100–580 mm/min (the selected interval was 160 mm/min), respectively. The milling length of each test was about 15–20 mm.

The workpiece was horizontally clamped on a frock clamp. In this clamping method, the ply orientation was parallel to the axis of the end mill. All of the experimental setups are shown in Fig. 7. The fiber whose axis was perpendicular to the feed direction was treated as fill fiber, namely the initial fiber orientation $\theta_0$ was 90°. So, the occurrence of the damages of the fill fibers was analyzed.

**Table 1** Material properties and feed rate used for model predictions [33, 34]

| Items | Value |
|---|---|
| Longitudinal Young's modulus of fiber, $E_1$ | 122.6 GPa |
| Transverse Young's modulus of fiber, $E_2$ | 7.7 GPa |
| Equivalent elastic modulus, $E$ | 2.3 GPa |
| Equivalent modulus of foundation, $k$ | $4.7 \times 10^{-4}$ N/mm$^3$ |
| Strain energy release rate of Mode I fracture, $G_{Ic}$ | 260 J/m$^2$ |
| Poisson's ratio, $\nu$ | 0.3 |
| Friction coefficient, $\mu$ | 0.3 |
| Fiber bonding strength, $\sigma_b$ | 390 MPa |
| Feed per tooth, $f_z$ | 0.1 mm/tooth |

## 4 Results and discussion

### 4.1 Effect of the initial fiber orientation $\theta_0$ on the occurrence of delamination and burrs

Using the above theoretical model, the critical fiber-cutting angles (i.e., $\varphi_{CT}$ and $\varphi_C$) and the corresponding engagement angle with different initial fiber orientation are predicted and compared with the results obtained by Voss et al. [8] as shown in Fig. 8. Their main experimental conditions were that the rake angle $\gamma_0 = 15°$, the clearance angle $\alpha = 14°$, the helix angle $\beta_b = 0°$, the peak radius $r_{peak} = 5$–$15$ μm, and the feed per tooth $f_z = 0.06$ mm/tooth.

During cutting, when the fiber is tangent to the flank face, the bending angle or the fiber cutting angle reaches the maximum value. Before this, the fiber fractures if the fiber cutting angle exceeds the critical one, namely $\varphi > \varphi_{CT}$. Then, the fiber can be removed. However, the fiber turns into a burr if the fiber-cutting angle does not exceed the critical one (i.e. $\varphi < \varphi_{CT}$), because the internal stress in the fiber induced by the bending cannot exceed the bending strength. In addition, for any initial fiber orientation, the fiber-cutting angle changes with the engagement angle changing during milling process. Within a certain range of the engagement angle, it can be sure that the fiber-cutting angle is always less than the critical one. Then, the significant burr areas may be observed within this range of engagement angle. These burr areas can be defined as burr occurrence zone (BOZ). The BOZ changes with the

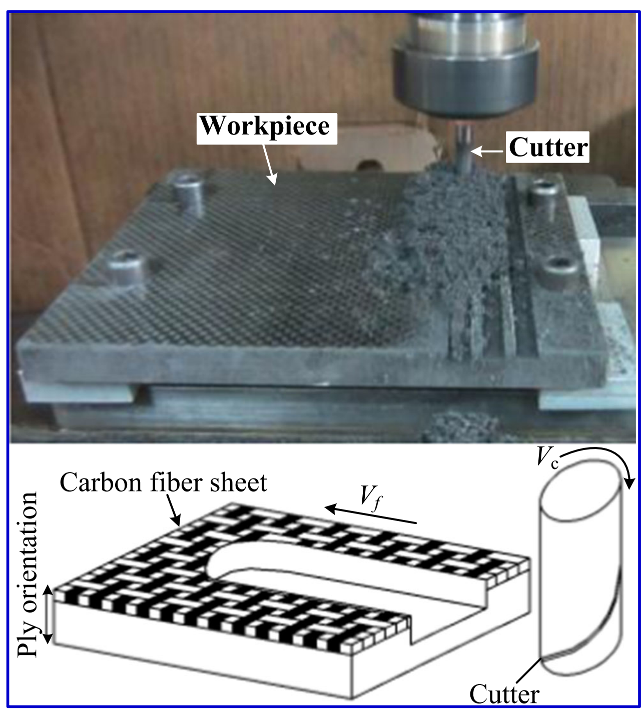


**Fig. 7** Experimental setup

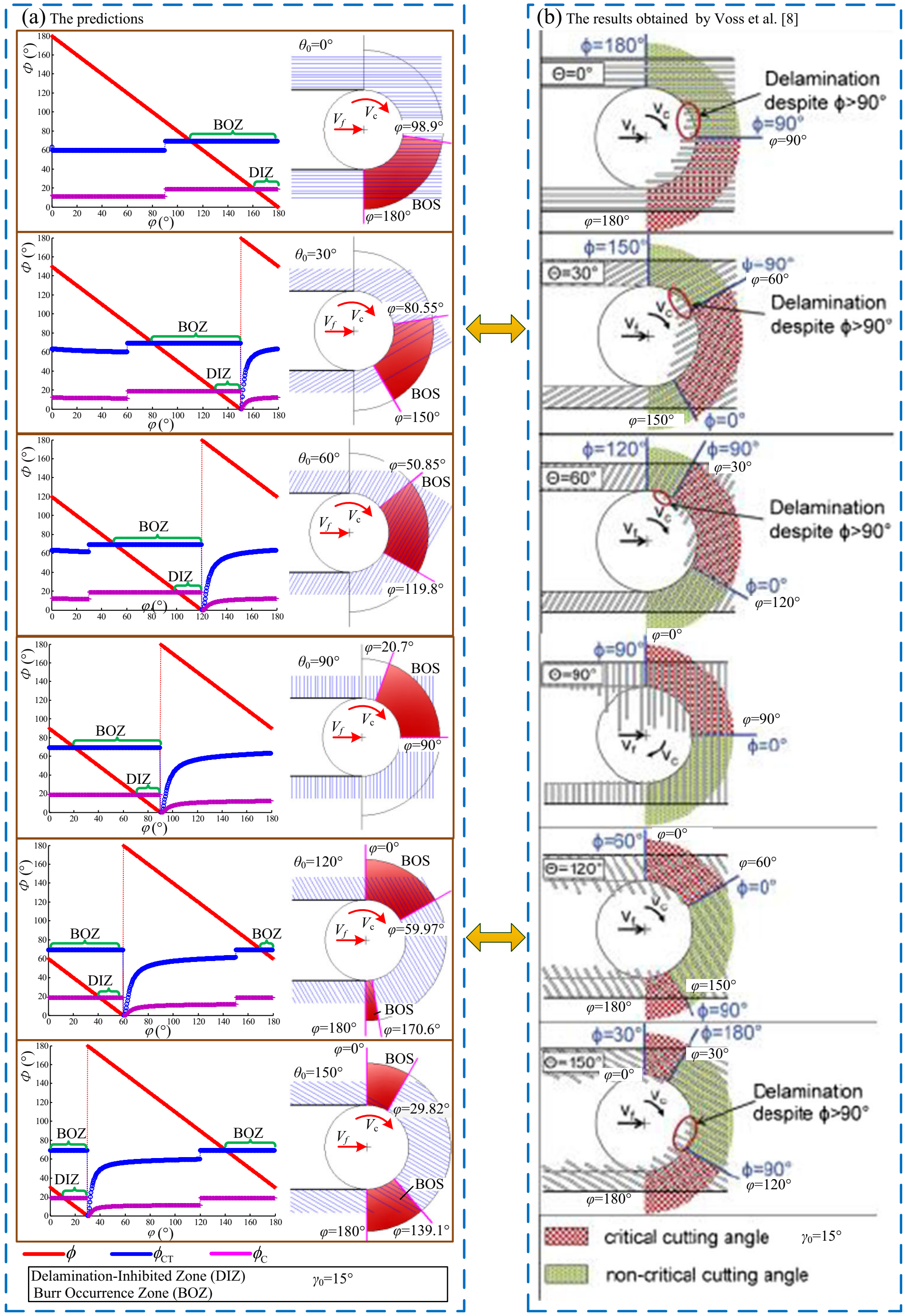


**Fig. 8** BOZs and DIZs with different initial fiber orientation, $\theta_0$

change in the engagement angle. Moreover, the fiber-cutting angle is highly dependent on the initial fiber orientation. So, the BOZ changes with the change in the initial fiber orientation. The BOZ for different initial fiber orientation is shown in Fig. 8, and the critical zones (BOZs) are marked red in the schematic illustration. The predicted variation of the fiber-cutting angle and its critical ones (i.e., $\varphi_{CT}$ and $\varphi_C$) with the engagement angle are shown in Fig. 8a, as well as the schematic illustrations. These model predictions and the results obtained by Voss et al. [8] (as shown in Fig. 8b) are compared and agree well with each other. Figure 8 demonstrates that the burrs with the initial fiber orientations $\theta_0 = 0°$, $\theta_0 = 120°$, and $\theta_0 = 150°$ are formed on or near the straight slot edges. These burrs cannot be removed after the cutting tool passed through during the formation of the straight slot edges. However, the burrs with the initial fiber orientations $\theta_0 = 30°$

and $\theta_0 = 60°$ are formed on the curve slot edge and away from the straight slot edges, and these burrs can be removed during the formation of the straight slot edges. Thereby, the burrs in these cases may be less than those in the former cases. These rules are consistent with the results observed by Voss et al. [8]. Therefore, in order to get the smoother slot edges, the suitable initial fiber orientations can be chosen in the range from 30° to 60°.

Additionally, as $\varphi > \varphi_C$, the delamination cracking occurs along the fiber axis caused by the loads $P_n$ and $P_t$. Conversely, the delamination cracking may be inhibited. From Fig. 8, it is evident that the delamination cracking can be prone to be created and exists throughout the whole cutting area. The delamination-inhibited zone (DIZ) is incredibly tiny and usually in the burr occurrence zone (BOZ).

## 4.2 Generation rules of the surface damages with the initial fiber orientation $\theta_0 = 90°$

Considering the initial fiber orientation $\theta_0 = 90°$ in Fig. 9, the variations of the fiber cutting angle $\varphi$ and the corresponding critical ones with the engagement angle $\varphi$ are proved.

When $0 < \varphi \leq \gamma_0 + \pi/2$ (here $\gamma_0 = 15°$), as shown in Fig. 9a, the fiber-cutting angle $\varphi$ gradually decreases from $\gamma_0 + \pi/2$ to 0 with the increase of the engagement angle $\varphi$. As shown in Fig. 9b and c, $\Delta\delta$ is gradually reduced from $r_e$ to 0 during the cutting, and the drop of the bending load $P$ appears. However, their variation ranges are all very small. As a result, the variation ranges of the critical fiber-cutting angles (i.e., $\varphi_{CT}$ and $\varphi_C$) are all so small, which could keep these critical angles at certain values (i.e., $\varphi_{CT} = 69.2°$ and $\varphi_C = 18.8°$). When $\varphi = \varphi_{CT} = 69.2°$, the engagement angle $\varphi = 20.7°$. As $0 \leq \varphi \leq 20.7°$, the fiber-cutting angle can exceed the critical one (namely, $\varphi \geq \varphi_{CT}$), and the fiber can be removed. However, when $20.7° < \varphi \leq 90°$, the fiber-cutting angle or the maximum bending angle cannot be over the critical one (namely $\varphi < \varphi_{CT}$), and the fiber cannot be removed, and turned into the burr. So, the range of $20.7° < \varphi \leq 90°$ is a burr occurrence zone (BOZ). In addition, as $\varphi = \varphi_C = 18.8°$, the engagement angle $\varphi = 71.1°$. As $0 \leq \varphi \leq 71.7°$, the fiber-cutting angle can exceed the critical one, and the delamination cracking can easily occur. However, when $71.1° < \varphi \leq 90°$, the delamination cracking can be restrained because $\varphi < \varphi_C$. Therefore, the range of $71.1° < \varphi \leq 90°$ is a delamination-inhibited zone (DIZ).

Likewise, when $\gamma_0 + \pi/2 < \varphi(\gamma_0 = 0)$ as shown in Fig. 9, the fiber-cutting angle $\varphi$ is gradually decreased from π to $\gamma_0 + \pi/2$ with the increase of the engagement angle $\varphi$. Both $\Delta\delta$ and $P$ are gradually decreased, but the variations of them are larger than when $0 < \varphi \leq \gamma_0 + \pi/2$. Hence, the critical angles (i.e., $\varphi_{CT}$ and $\varphi_C$) obviously change. However, both $\varphi_{CT}$ and $\varphi_C$ are far below the fiber-cutting angle. Thereby, the fiber can be effectively removed as $\gamma_0 + \pi/2 < \varphi$, but the delamination cracking may be prone to be formed.

In summary, based on the above theoretical model analyses, it is demonstrated that the range of $20.7° < \varphi \leq 90°$ is a burr occurrence zone (BOZ) when the initial fiber orientation $\theta_0 = 90°$. In addition, the range of $71.1° < \varphi \leq 90°$ is a delamination-inhibited zone (DIZ), and this zone is within the burr occurrence zone (BOZ).

The warp yarns and the fill yarns in the plain weave fabric cannot be able to be distinguished after the forming of CFRP. In order to be easily distinguished, the fiber whose axis is parallel to the feed direction is regarded as warp fiber, namely the initial fiber orientation $\theta_0 = 0°/180°$. The fiber whose axis is perpendicular to the feed direction is treated as fill fiber, then the initial fiber orientation $\theta_0 = 90°$ in this case. To examine the validity of the results of the theoretical model when $\theta_0 = 90°$, several milling experiments are conducted. The workpiece is horizontally clamped on a frock clamp in these experiments. Figure 10 depicts the machining effects of part experiments with different cutting parameters. As displayed in Fig. 10, there are some warp burrs or even the mixed burrs of the fill burrs and the warp burrs on the top layer. Furthermore, the delamination cracking is widespread on the top layer and often covered by the burrs, resulting in the inhibitive effect on

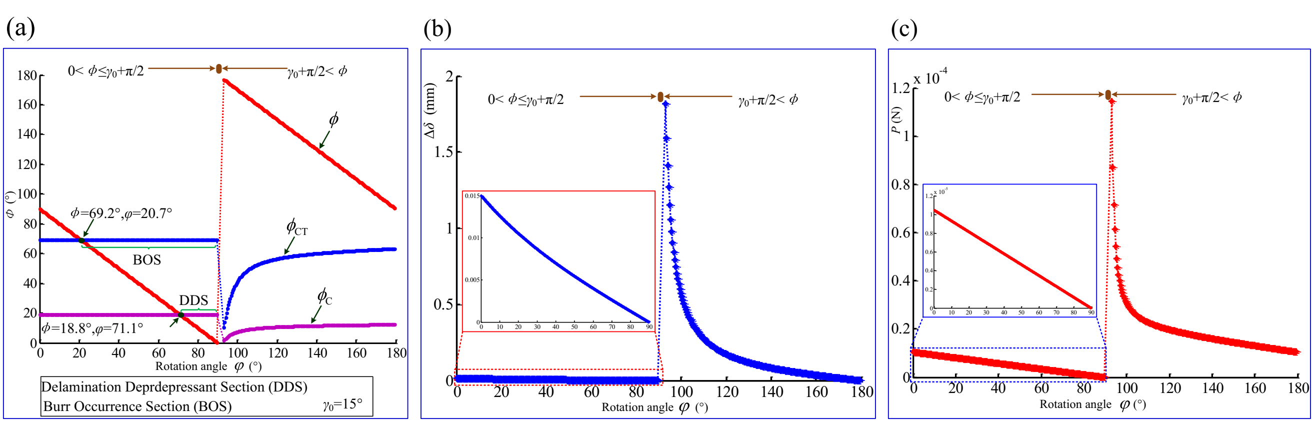


Fig. 9 Variations of $\varphi_{CT}$, $\varphi_C$, $P$, and $\Delta\delta$ with $\varphi$ (when $\theta_0 = 90°$)

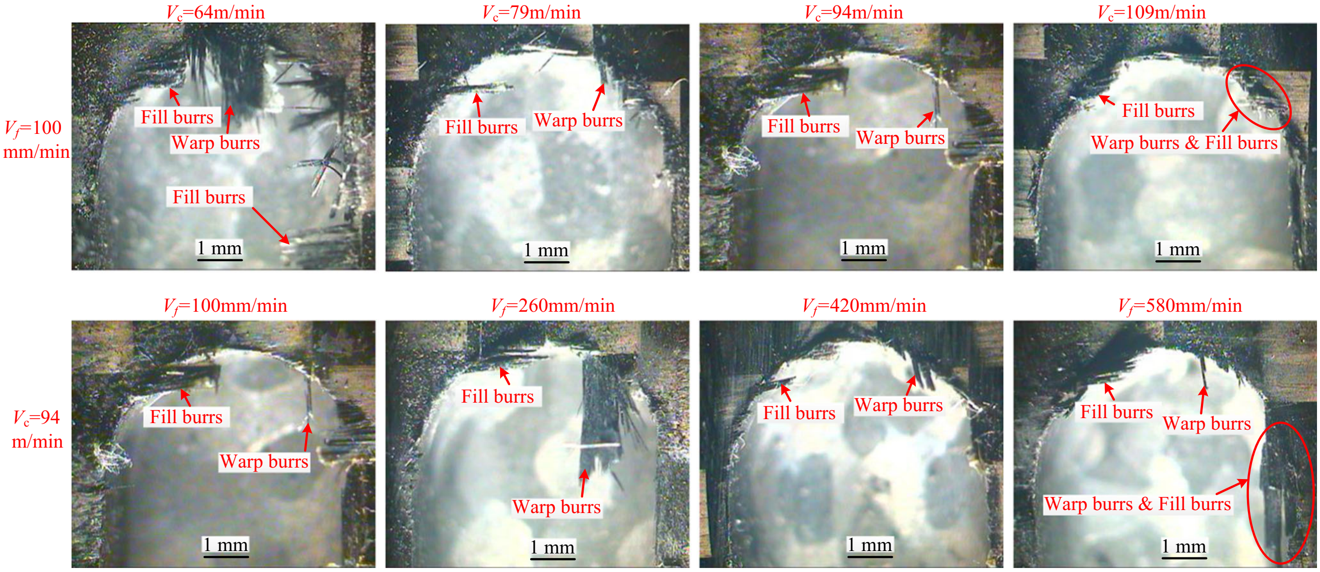


**Fig. 10** Machining effects with different cutting parameters (when $\theta_0 = 90°$)

the delamination cracking is not suitable to be observed. However, it clearly demonstrates the same occurrence regularity of the burrs in all the machining effects. Therefore, combining the calculational results, the research may put emphasis on analyzing the occurrence of the damages of the fill yarns, especially the occurrence of fill burrs, in the following subsections.

Figure 11 shows the images of the slot surface at $V_c = 94$ m/min, $V_f = 100$ mm/min, and $a_p = 3$ mm. A dotted yellow line is used to mark the margin of the delamination in Fig. 11. There are so many obvious fill burrs induced from the fill fibers when $29.8° \leq \varphi \leq 90°$ and $\varphi = 180°$ as shown in Fig. 11. Therefore, the ranges of $29.8° \leq \varphi \leq 90°$ and $\varphi = 180°$ are the burr occurrence zones (BOZs). It is also shown that the delamination is reduced when $67.7° \leq \varphi < 90°$, and this range is regarded as a delamination-inhibited zone (DIZ). These results are basically consistent with the theory deduction.

Theoretically, there are no burrs as $\varphi = 180°$, because the fiber-cutting angle can exceed the critical one, and the fiber can be removed in or near this engagement angle range. However, the burrs appear in this engagement angle range in actual processing. Noteworthy, it can be known that the engagement angle $\varphi = 0°$ is at the beginning of tool engagement and the engagement angle $\varphi = 180°$ is at the tooth exit. At the beginning of tool engagement, the cut depth gradually increases from zero. The supporting effect imposed by the uncut layers is strong. In addition, because of the woven structure, the warp fibers and the fill fibers are separated from each other, and constrained by each other. As a result, the fiber-bending deflection which is perpendicular to the workpiece surface may be decreased. On the contrary, the supporting effect and the confinement effect are all reduced significantly because the cut depth decreases gradually to zero. Then, the perpendicular bending deflection of the fiber may be easy to occur. In general, the fiber is always under the combined condition of the local contact stress and bending stress in cutting area. The tool–fiber contact can be treated as elliptical Hertzian contact problem. The tool–fiber contact at the

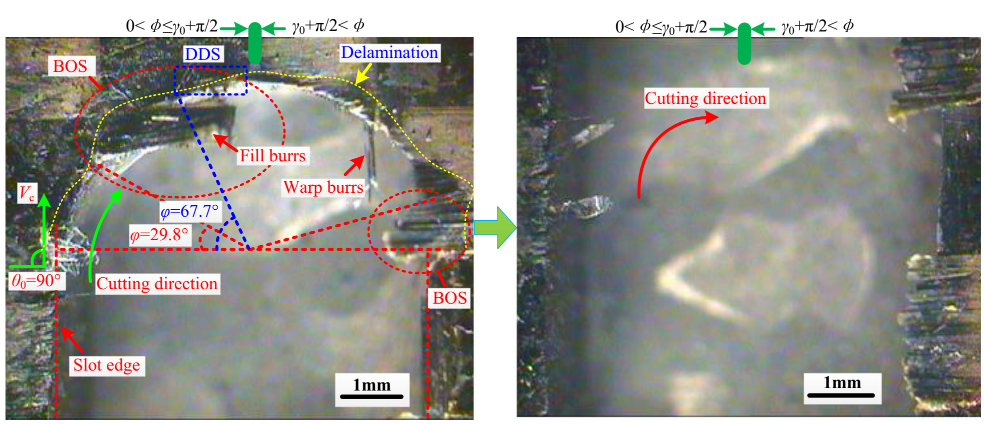


**Fig. 11** Surfaces of the slot edges ($V_c = 94$ m/min, $V_f = 100$ mm/min, $a_p = 3$ mm)

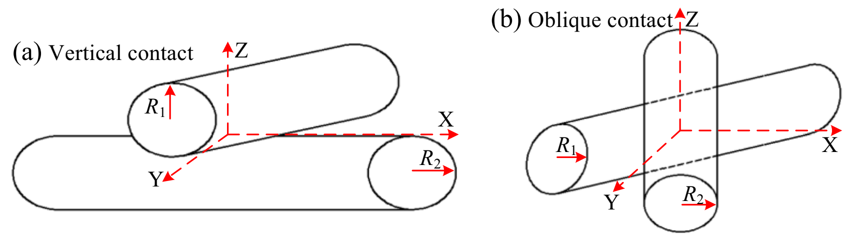


**Fig. 12** Tool–fiber contact models (when $\varphi = 0°$ or $\varphi = 180°$)

beginning of tool engagement ($\varphi = 0°$) is equivalent to that between two cylinders of similar radius with $\pi/2$ crossed axes, due to the small perpendicular bending deflection of the fiber. By contrast, the contact between the fiber and the cutting edge at the tooth exit ($\varphi = 180°$) is also equivalent to that between two cylinders, but the angle between their central axes is less than $\pi/2$. Here, it is assumed that this angle is $\pi/4$. The contact models of the two cases are illustrated in Fig. 12. The maximum pressure occurs at the center of the contact area and that of the two cases are given by [11]:

$$\begin{cases} F_p = \dfrac{4}{3}E^*\sqrt{\overline{R}d_\Delta^3} \\ F_o = \dfrac{2\sqrt[4]{2}}{3}E^*\sqrt{\overline{R}d_\Delta^3} \end{cases} \tag{36}$$

where $\frac{1}{E^*} = \frac{1}{E^*} + \frac{1}{E^*}$, $\overline{R}$ is the equivalent radius, $\frac{1}{\overline{R}} = \frac{1}{R} + \frac{1}{R}$, $R_1$ and $R_2$ are the cutting edge radius and the fiber radius, respectively.

According to Eq. (36), there is a difference of factor 0.59 ($F_o/F_p = 0.59$) between these two pressures with the same tool and material parameters. Due to the phenomenon that the fibers evade the tool edge by the upward bending of the fiber, the maximum pressure of the latter case can be obviously decreased, leading to the lower shearing crack possibility of the fiber and the larger buckling deflection. As a result, the slot edge burrs at the tooth exit are more obvious than that at the beginning of tool engagement. It is a reason that the ranges of $\varphi = 180°$ is another burr occurrence zone (BOZ) in actual processing.

Moreover, as $0 \le \varphi \le \gamma_0 + \pi/2$, the burrs are formed on the curve slot edge and away from the straight slot edge, so these burrs can be removed during the formation of the straight slot edges. Nevertheless, the burrs cannot be removed at $\varphi = 180°$ when $\gamma_0 + \pi/2 < \varphi$, because the burrs are on or near the straight slot edge. Thus, the burrs at the tooth exit are more obvious than that at the beginning of tool engagement. When $\theta_0 = 90°$, the region when the engagement angle lies in $0 \le \varphi \le \pi/2$ is within the up-milled zone, and the other region when $\pi/2 < \varphi \le \pi$ is within the down-milled zone. It can be seen that the burr defect on the down-milled edge is more severe than that on up-milled edge. Therefore, when $\theta_0 = 90°$, it is beneficial to reduce the burrs and improve the machining quality of the slot surface with up-milling in actual machining process.

## 5 Conclusions

Top-layer damages, such as burrs and delamination, are some of the crucial quality issues in CFRP milling. In this paper, the theoretical models for revealing the mechanisms of these damages formation have been proposed based on the elastic foundation beam theory. The occurrence of these damages with different initial fiber orientation has been investigated. Some key conclusions are drawn from the results presented in this research as follows:

(1) The initial fiber orientation directly affects the burrs and delamination distributions during the milling of CFRP. To reduce the burrs and get the smoother slot edges, the suitable initial fiber orientations may be chosen in the range of 30° to 60°;
(2) As $\theta_0 = 90°$, there are two burr occurrence zones (BOZs) (i.e., $29.8° \le \varphi \le 90°$ and $\varphi = 180°$);
(3) When $\theta_0 = 90°$, the burr defect on the down-milled edge is more severe than that on up-milled edge. Therefore, the milling quality of the slot surface can be improved under the up-milling operation.

From Eqs. (1), (17), (22), (33), (35), and (36), it is proved that there are many factors, such as the feed rate, the cutting edge radius $r_e$, the rake angle, and the tool–fiber contact state, affecting the occurrences of the top-layer damages. In further studies, according to these models, the effects of the feed rate, the tool wear, the tool geometry, the tool–fiber contact state on the occurrences of the damages (i.e., burrs and delamination) will be studied in detail.

**Acknowledgements** Special thanks to the National Science Foundation of China (No. 51675285) for funding this work.

## References

1. Bonnet C, Poulachon G, Rech J, Girard Y, Costes JP (2015) CFRP drilling: fundamental study of local feed force and consequences on hole exit damage [J]. Int J Mach Tools Manuf 94:57–64
2. Jia Z, Fu R, Niu B et al (2016) Novel drill structure for damage reduction in drilling CFRP composites [J]. Int J Mach Tools Manuf 110:55–65
3. Karpat Y, Değer B, Bahtiyar O (2014) Experimental evaluation of polycrystalline diamond tool geometries while

drilling carbon fiber-reinforced plastics [J]. Int J Adv Manuf Technol 71(5–8):1295–1307

4. Karpat B (2015) Tool geometry based prediction of critical thrust force while drilling carbon fiber reinforced polymers [J]. Adv Manuf 3(4):300–308
5. Xu W, Zhang LC, Wu Y (2014) Elliptic vibration-assisted cutting of fibre-reinforced polymer composites: understanding the material removal mechanisms [J]. Compos Sci Technol 92(3):103–111
6. Hintze W, Hartmann D, Schütte C (2011) Occurrence and propagation of delamination during the machining of carbon fibre reinforced plastics (CFRPs)—an experimental study [J]. Compos Sci Technol 71(15):1719–1726
7. Wang FJ, Yin JW, Ma JW et al (2017) Effects of cutting edge radius and fiber cutting angle on the cutting-induced surface damage in machining of unidirectional CFRP composite laminates [J]. Int J Adv Manuf Technol 91(9–12):3107–3120
8. Voss R, Seeholzer L, Kuster F, Wegener K (2017) Influence of fibre orientation, tool geometry and process parameters on surface quality in milling of CFRP [J]. CIRP J Manuf Sci Technol 18:75–91
9. Ghafarizadeh S, Chatelain JF, Lebrun G (2016) Finite element analysis of surface milling of carbon fiber-reinforced composites [J]. Int J Adv Manuf Technol 87(1–4):399–409
10. Li H, Qin X, He G, Price MA, Jin Y, Sun D (2017) An energy based force prediction method for UD-CFRP orthogonal machining [J]. Compos Struct 159:34–43
11. Su Y, Jia Z, Niu B, Bi G (2017) Size effect of depth of cut on chip formation mechanism in machining of CFRP [J]. Compos Struct 164:316–327
12. Xu W, Zhang LC (2014) On the mechanics and material removal mechanisms of vibration-assisted cutting of unidirectional fibre-reinforced polymer composites [J]. Int J Mach Tools Manuf 80–81(5):1–10
13. Xu W, Zhang L (2016) Mechanics of fibre deformation and fracture in vibration-assisted cutting of unidirectional fibre-reinforced polymer composites [J]. Int J Mach Tools Manuf 103:40–52
14. Gaugel S, Sripathy P, Haeger A, Meinhard D, Bernthaler T, Lissek F, Kaufeld M, Knoblauch V, Schneider G (2016) A comparative study on tool wear and laminate damage in drilling of carbon-fiber reinforced polymers (CFRP) [J]. Compos Struct 155:173–183
15. Voss R, Henerichs M, Harsch D et al (2016) Optimised approach for characterisation of cutting edge micro-geometry in drilling carbon fibre reinforced plastics (CFRP) [J]. Int J Adv Manuf Technol 90(1–4):1–16
16. Hintze W, Hartmann D (2013) Modeling of delamination during milling of unidirectional CFRP [C]. Procedia CIRP 8:444–449
17. Jia ZY, Su YL, Niu B et al (2016) The interaction between the cutting force and induced sub-surface damage in machining of carbon fiber-reinforced plastics [J]. J Reinf Plast Comp 35(9):712–726
18. Colligan K, Ramulu M (1991) Delamination in surface plies of graphite/epoxy caused by the edge trimming process [J]. Process Manuf Compos Mater 27:113–125
19. Sheikh-Ahmad J, Urban N, Cheraghi H (2012) Machining damage in edge trimming of CFRP [J]. Mater Manuf Process 27(7):802–808
20. Zhou JW, Chen Y, Fu YC et al (2015) Influence of fiber cutting angle on the machining defects during slotting of CFRP [J]. J Harbin Inst Technol 47(7):110–116
21. Islam F, Ramkumar J, Milani AS (2016) A simplified damage prediction framework for milling of unidirectional carbon fiber-reinforced plastics [J]. Adv Manuf Polym Compos Sci 1(4):175–184
22. Davim JP, Reis P (2005) Damage and dimensional precision on milling carbon fiber-reinforced plastics using design experiments [J]. J Mater Process Tech 160:160–167
23. Chibane H, Morandeau A, Serra R, Bouchou A, Leroy R (2013) Optimal milling conditions for carbon/epoxy composite material using damage and vibration analysis [J]. Int J Adv Manuf Technol 68(5–8):1111–1121
24. Erkan Ö, Işık B, Çiçek A et al (2013) Prediction of damage factor in end milling of glass fibre reinforced plastic composites using artificial neural network [J]. Appl Compos Mater 20(4):517–536
25. Ghidossi P, Mansori ME, Pierron F (2004) Edge machining effects on the failure of polymer matrix composite coupons [J]. Compos Appl Sci Manuf 35(7–8):989–999
26. Niu B, Su Y, Yang R et al (2016) Micro–macro-mechanical model and material removal mechanism of machining carbon fiber reinforced polymer [J]. Int J Mach Tools Manuf 111:43–54
27. Wang H, Qin X (2016) A mechanistic model for cutting force in helical milling of carbon fiber-reinforced polymers [J]. Int J Adv Manuf Technol 82(9–12):1485–1494
28. Kalla D, Sheikh-Ahmad J, Twomey J (2010) Prediction of cutting forces in helical end milling fiber reinforced polymers [J]. Int J Mach Tools Manuf 50(10):882–891
29. Karpat Y, Bahtiyar O, Değer B (2012) Mechanistic force modeling for milling of unidirectional carbon fiber reinforced polymer laminates [J]. Int J Mach Tools Manuf 56(2):79–93
30. Beer FP, Russell Johnston E, Dewolf JT et al (2012) Mechanics of materials [M]. McGraw-Hill, New York
31. Jia JQ, Wang HT, Tu BX et al (2010) Analytical approach and field monitoring for mechanical behaviors of pipe roof reinforcement [J]. Rock Soil Mech 31(6):1858–1864
32. Jiao GQ, Xu JY (1995) Model I interlaminar fracture toughness and initial crack length of the composite materials [J]. Chin J Appl Mech 12(2):47–51
33. Qi Z, Zhang K, Cheng H, Wang D, Meng Q (2015) Microscopic mechanism based force prediction in orthogonal cutting of unidirectional CFRP[J]. Int J Adv Manuf Technol 79(5–8):1209–1219
34. Li G (2011) Research on defects generation mechanism and process optimization in drilling laminated composite [D]. Shandong University, Ji Nan
35. Sánchez NF, Díaz-Álvarez A, Cantero JL et al (2015) Experimental analysis of special tool geometries when drilling woven and multi-directional CFRPs [J]. J Reinf Plast Compos 19(19):1215–1220